

## Article

# Machine Learning-Based Multi-Level Fusion Framework for a Hybrid Voltammetric and Impedimetric Metal Ions Electronic Tongue

Tianqi Lu <sup>†</sup> , Ammar Al-Hamry <sup>†</sup> , Junfeng Hao , Yang Liu, Yunze Qu  and Olfa Kanoun <sup>\*</sup> 

Measurement and Sensor Technology, Department of Electrical Engineering and Information Technology, Chemnitz University of Technology, 09107 Chemnitz, Germany

<sup>\*</sup> Correspondence: olfa.kanoun@etit.tu-chemnitz.de<sup>†</sup> These authors contributed equally to this work.

**Abstract:** Electronic tongues and artificial gustation for crucial analytes in the environment, such as metal ions, are becoming increasingly important. In this contribution, we propose a multi-level fusion framework for a hybrid impedimetric and voltammetric electronic tongue to enhance the accuracy of  $K^+$ ,  $Mg^{2+}$ , and  $Ca^{2+}$  detection in an extensive concentration range (100.0 nM–1.0 mM). The proposed framework extracts electrochemical-based features and separately fuses, in the first step, impedimetric features, which are characteristic points and fixed frequency features, and the voltammetric features, which are current and potential features, for data reduction by LDA and classification by kNN. Then, in a second step, a decision fusion is carried out to combine the results for both measurement methods based on Dempster–Shafer (DS) evidence theory. The classification results reach an accuracy of 80.98% and 81.48% for voltammetric measurements and impedimetric measurements, respectively. The decision fusion based on DS evidence theory improves the total recognition accuracy to 91.60%, thus realizing significantly high accuracy in comparison to the state-of-the-art. In comparison, the feature fusion for both voltammetric and impedimetric features in one step reaches an accuracy of only 89.13%. The proposed hierarchical framework considers for the first time the fusion of impedimetric and voltammetric data and features from multiple electrochemical sensor arrays. The developed approach can be implemented for several further applications of pattern fusion, e.g., for electronic noses, measurement of environmental contaminants such as heavy metal ions, pesticides, explosives, and measurement of biomarkers, such as for the detection of cancers and diabetes.

**Keywords:** electronic tongue; metallic ions detection; sensor array fusion; voltammetric sensor array; impedimetric sensor array; decision fusion; chemometrics; smart agriculture



**Citation:** Lu, T.; Al-Hamry, A.; Hao, J.; Liu, Y.; Qu, Y.; Kanoun, O. Machine Learning-Based Multi-Level Fusion Framework for a Hybrid Voltammetric and Impedimetric Metal Ions Electronic Tongue. *Chemosensors* **2022**, *10*, 474. <https://doi.org/10.3390/chemosensors10110474>

Academic Editors: Hailong Wu and Tong Wang

Received: 13 October 2022

Accepted: 10 November 2022

Published: 12 November 2022

**Publisher's Note:** MDPI stays neutral with regard to jurisdictional claims in published maps and institutional affiliations.



**Copyright:** © 2022 by the authors. Licensee MDPI, Basel, Switzerland. This article is an open access article distributed under the terms and conditions of the Creative Commons Attribution (CC BY) license (<https://creativecommons.org/licenses/by/4.0/>).

## 1. Introduction

Potassium, calcium, and magnesium are essential metal elements for plant growth [1]. They are highly demanded as nutrient solutions, fertilizers, or supplements to enhance the yield and quality of crops in modern agriculture [2]. Potassium is a macronutrient for plant growth and is related to the movement of water and carbohydrates in plant tissues [3]. Calcium and magnesium are secondary nutrients for plants and have proven to be essential nutrient sources for photosynthesis [4], cell wall construction [5], and second messenger [6]. Their cationic forms ( $K^+$ ,  $Ca^{2+}$ , and  $Mg^{2+}$ ) are required to be precisely optimal and controlled in the plant growth environment to match the nutrient requirements of the crop under different growth stages [7–9]. Therefore, high-precision  $K^+$ ,  $Mg^{2+}$ , and  $Ca^{2+}$  quantification technologies combined with the Internet of Things (IoT) are widely used in aquaponics [10], soilless cultivation [11], smart fisheries [12], and automatic agriculture [13].

With the development and increased demand for smart agriculture, there are many objective requirements for high-accuracy ion detection in a rapid, portable, and cost-effective manner [7]. Classical ion detection techniques are costly and rely on large equipment, unsuitable for online measurement and IoT adaptation, such as complexation titration [14], ion chromatography [15], mass spectrometry [16], spectroscopy [17], and spectrophotometry [18]. Therefore, microsensor techniques combining sensitive materials have been applied for rapid ion detection as valued methods, such as voltammetric sensors [19–21], impedimetric sensors [22,23], and potentiometric sensors [24], which could enable reliable integration with portable measurement devices. Gruden and Kanoun [25,26] demonstrated that cyclic voltammetry (CV) could be employed to discriminate the ratio of  $\text{Ca}^{2+}$  and  $\text{Mg}^{2+}$  in water and further developed a cost-effective sensor system combining electrochemical impedance spectroscopy (EIS) and CV for the online determination of aqueous solutions. Peng et al. [27] prepared an electrochemical sensor based on  $\text{NiS}_2$  nanoparticles (NPs) for the detection of  $\text{Ca}^{2+}$  and  $\text{Mg}^{2+}$  in water with a detection range of 1 nM–100 nM. Kumbhat et al. [28] developed an electrochemical sensor based on a self-assembled monolayer of 4-aminobenzo-18-Crown-6 ether as a selective ionophore for highly selective  $\text{K}^+$  (1  $\mu\text{M}$ –10 mM) detection. For impedimetric detection, Akhter et al. [29] reported a 3D-printed impedimetric sensor based on multi-walled carbon nanotubes, which can recognize  $\text{Ca}^{2+}$  and  $\text{Mg}^{2+}$  between 1 ppm and 200 ppm. Machado et al. [30] fabricated an impedimetric multichannel monolayer-coated gold sensor to detect low concentration change in  $\text{K}^+$  in mouse brains. In summary, a large number of studies regarding sensitive material-based sensors demonstrated their critical role and potential in the field of ion detection. However, a single sensor is generally only applicable to the detection of one single kind of ion, whereas the desired high detection accuracy is difficult to be achieved for complex multi-analyte detection scenarios. This is limited by the limitation of the sensing principle itself.

Multi-sensor array for detecting analytes in liquids is defined as an electronic tongue (E-Tongue; ET) and received considerable attention during the last two decades due to its potential for analyzing multiple analytes and the IoT-integration possibility [31]. ET can emulate the taste mechanism of humans and can perform highly accurate ion classification and identification using response signals toward the target ions to establish specific fingerprints. Generally, ET consists of a sensor array for chemical detection and an advanced pattern recognition system to extract holistic features from complex samples to identify target analytes [32]. Riul et al. [33,34] first proposed that an ET based on a conductive polymer impedimetric sensor array (ISA) can be employed to detect metal ions in water. Cortina-Puig et al. [35] reported an ionophore/polypyrrole-based impedimetric ET that can simultaneously quantitatively recognize potassium, sodium, and ammonium ions. Pérez-Ràfols et al. [36] developed an ET based on voltammetric sensor array (VSA) for several metallic ions discrimination by employing differential pulse anodic stripping voltammetry (DPASV) and partial least squares regression (PLSR). Men et al. [37] reported dual-ET containing chalcogenide-based voltammetric sensors to detect metal ions in wastewater and seawater. The above contributions demonstrated the feasibility of the ET technique in the field of ion detection. The advantage of ET compared with using a single sensor to detect ions is that sensor arrays bring new dimensions to the observation, contributing to the analysis based on more parameters and improving predictive performance.

Pattern fusion is an essential strategy in a multi-sensor system, aiming to achieve higher accuracy recognition results by different sensor combinations to obtain response information of analytes from multiple perspectives, such as a combination of ET and electronic nose (EN) [38], combination of computer vision and pressure sensor array [39], and hybrid sensor array of different sensing techniques. The pattern fusion strategy includes data fusion, feature fusion, and decision fusion. Data fusion is low-level fusion aiming to fuse raw data and extract or calculate less valuable data. Feature fusion is intermediate-level fusion and is applied for the fusion of features extracted by different algorithms to characterize the response signal of analytes comprehensively. Decision fusion is high-level

fusion, which can integrate established decisions from multiple determination channels (classifiers) to achieve high accuracy final decision based on various considerations [40,41]. The combination of voltammetric and potentiometric ET has proved to be effective in detecting or discriminating beers [42], fermented milk [43], aspergillus of food [44], and apple extracts [45]. Labrador et al. [46] proposed a hybrid ET combining a VSA and a single impedimetric sensor for composition analysis of minced meat. Therefore, the combination of sensor arrays with different sensing techniques enhances recognition accuracy and provides more evidence for classification.

This contribution firstly proposes a multi-fusion strategy framework for an electronic tongue-based VSA and ISA to exploit their synergy and enhance, thereby, the measurement accuracy of the concentrations of  $K^+$ ,  $Mg^{2+}$ , and  $Ca^{2+}$  in liquid samples in the range from 100.0 nM to 1.0 mM. The developed electronic tongue consists of four voltammetric sensors and six impedimetric sensors. We proposed to extract electrochemical-based features, which are relevant to the corresponding measurement method, and to realize a hybrid feature fusion (intermediate-level fusion) for every method separately, followed by a decision fusion (high-level fusion) combining both results, as shown in Figure 1. The effectiveness of the extracted features was evaluated. A supervised dimensionality reduction algorithm was applied to analyze the effect of cluster scatters on the extracted features. The  $k$ -nearest neighbor (kNN) classifier was employed to classify the clusters under multiple dimensionalities. The evidence theory algorithm fused the decision results of the VSA and ISA to enhance the prediction accuracy of the final decision. Recognition results based on different algorithms and fusion strategies were compared.

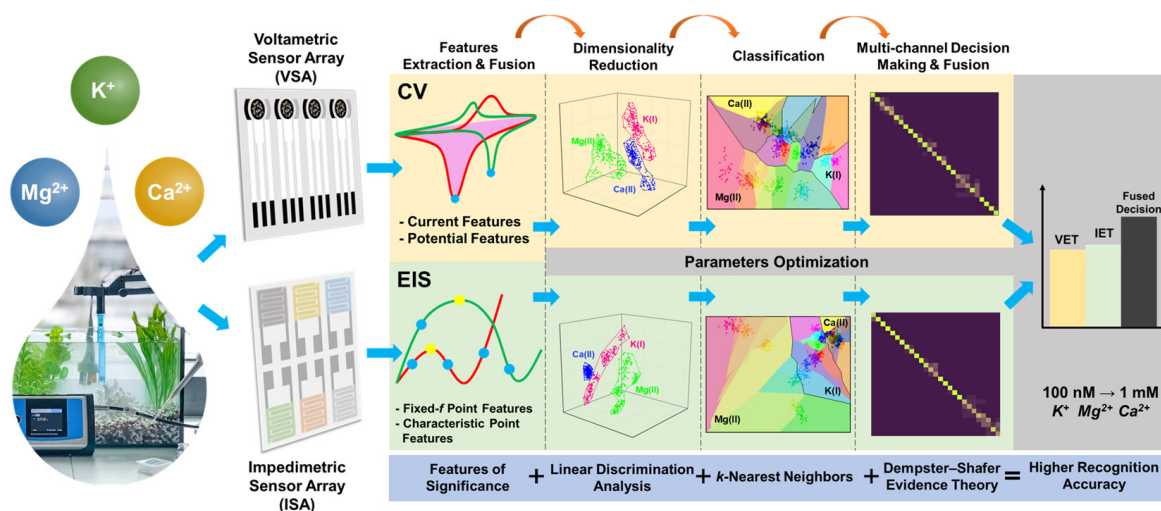


**Figure 1.** Concept of the proposed multi-level fusion framework for a hybrid voltammetric and impedimetric electronic tongue for metal ions detection.

## 2. Experiments and Methods

### 2.1. Sample Preparation

The samples containing metallic ions were prepared by dissolving the chloride salt ( $KCl$ ,  $MgCl_2$ ,  $CaCl_2(H_2O)_2$ ) powder in phosphate buffer solution (PBS) (0.1 M, pH = 7.0) and then sonicated for 1 h using an ultrasonic bath to ensure solubilization. The applied chloride salts were purchased from Sigma-Aldrich (Sigma Chemical Co., St. Louis, MO, USA; Aldrich Chemical Co., Milwaukee, WI, USA). Nine concentrations (100.0 nM, 500.0 nM, 1.0  $\mu$ M, 5.0  $\mu$ M, 10.0  $\mu$ M, 50.0  $\mu$ M, 100.0  $\mu$ M, 500.0  $\mu$ M, 1.0 mM) of samples were prepared for each metallic ion. Thirty samples of each metallic ion and each above concentration were prepared, 810 samples in total. The samples were individually stored in glass bottles at room temperature.

## 2.2. Voltammetric Measurements

A VSA was applied for the voltammetry measurement of the samples, which consists of four voltammetric sensors based on metal NPs electrochemical deposition layer and modified with metallic phthalocyanine (MPc) and COOH-functionalized multi-walled carbon nanotubes (MWCNT-COOH), preparation details are provided in Table S1. The sensors were based on commercial carbon screen-printed electrodes (Itasens IS-C, PalmSens BV, Houten, The Netherlands) with a paper substrate. The well-prepared sensor array is shown in Figure S1A.

The measurements were executed by PalmSens4 Electrochemical Workstation (PalmSens BV, Houten, Netherland) with the following procedure: 1 mL of sample was dropped on the working area of each sensor by pipette, then left for 30 s. CV was carried out with a scan range between  $-0.9$  V and 0 V and 0.005 V of scan step length, and only the reduction curve with 179 points was selected to extract features. The sensors were cleaned with deionized water for 30 s after measurement, then dried under air flow for 1 min. For continuous measurements, samples of the same concentration of different ions are selected for cross-measurement to avoid sensor fatigue for the same ion. The schematic diagram of the voltammetric measurement is shown in Figure S1B.

## 2.3. Impedimetric Measurements

An ISA was applied to the EIS measurement of the samples, which consists of six impedimetric sensors modified with composite films of poly(3,4-ethylenedioxythiophene)-polystyrene sulfonate (PEDOT:PSS), MPc, and MWCNT-COOH, and the preparation details are given in Table S2. The electrodes are silver screen-printed interdigitated electrodes (IDEs) on a polyimide (PI) substrate. The well-prepared sensor array is shown in Figure S2A. Generally, impedimetric sensors demonstrate relatively lower specific detection ability compared to voltammetric sensors; thus, the ISA has more numbers of sensors than the VSA in this contribution. The measurement was executed by Agilent 4294A Precision Impedance Analyzer (Agilent Technologies Inc., Santa Clara, CA, USA). The impedance response toward samples was acquired 201 points from the frequency range between 40 Hz and 110 MHz. Other operations are the same as voltammetric measurement. The schematic diagram of the impedimetric measurement is shown in Figure S2B.

## 2.4. Pattern Fusion Framework

### 2.4.1. Features Extraction and Fusion

Usually, the raw signals of sensors are not used directly for analysis because the noise and redundancy of the data increase the calculation difficulty for portable measurements. Feature extraction is employed to extract signals corresponding to physical or chemical processes and reduces the amount of data computation [47]. Feature extraction of VSA and ISA represent different aspects of the response toward metal ions.

Voltammetric measurements usually apply a continuously varying potential to obtain an I-V curve of the sensor to the target analyte to demonstrate the oxidation or reduction reaction reacting on the surface of the working electrode. The shape of the I-V curve mainly depends on the modification of the working electrode and the redox properties of the analyte. The potential information in the curves represents the potential at which the oxidation or reduction reaction occurs and is employed for the qualitative identification of the target analyte. The current information exhibits a strong correlation with the concentration of the target analyte and is usually utilized to identify the concentration of the analyte in the sample [48]. In this study, the data from the reduction part of CV curves were utilized for feature extraction.

The features based on the current information are the reduction current peak (RC) and reduction curve integral (RI) of the sensor in VSA response towards the target ions, as presented in Equations (1) and (2), respectively:

$$RC_i = I_{i,n} \quad (i = 1, 2, \dots, 4 \text{ for VSA}) \quad (1)$$

$$RI_i = \sum_{k=1}^{179} I_{i,k} \quad (i = 1, 2, \dots, 4 \text{ for VSA}) \quad (2)$$

where  $n$  is the number of the reduction peak point,  $i$  is the sensor label in VSA,  $I$  is the current value of the acquired data point, and  $k$  is the number of each acquired point on the reduction part of the CV curve.

The feature based on potential information is the potential value at the reduction peak (RP) as presented in Equation (3):

$$RP_i = V_{i,n} \quad (i = 1, 2, \dots, 4 \text{ for VSA}) \quad (3)$$

where  $V$  is the potential value of the reduction peak point, and other variables are the same as in Equations (1) and (2).

EIS characterizes and analyzes electrochemical properties such as electrode process kinetics, bilayer, and diffusion by measuring impedance variation with sinusoidal frequency. Nyquist plot was used to visualize EIS for analyzing properties of the electrochemical system, such as equivalent circuits, by plotting the x- and y-axis as the real part ( $Z'$ ) and imaginary part ( $Z''$ ) of impedance, respectively. Each point therein represents the impedance information of this system at a fixed frequency; however, the relative position of this point in the plot may change depending on the analyte [25,49,50]. Therefore, a complete description of the sensor's response toward the analyte can be obtained by extracting and combining the impedance information of the points at specific positions or specific frequencies.

The features based on the information of the characteristic points are the real part ( $CP_{peak-Z'}$ ) and imaginary ( $CP_{peak-Z''}$ ) part of the impedance at the peak characteristic point of the charge-transfer semi-circle in the Nyquist plot of the sensor response to the target ion in the ISA as Equations (4) and (5), respectively:

$$CP_{peak-Z',i} = R_{i,n} \quad (i = 1, 2, \dots, 6 \text{ for ISA}) \quad (4)$$

$$CP_{peak-Z'',i} = X_{i,n} \quad (i = 1, 2, \dots, 6 \text{ for ISA}) \quad (5)$$

where  $n$  is the number of the peak characteristic point of the charge-transfer semi-circle,  $i$  is the sensor label in ISA, and  $R$  and  $X$  are the real and imaginary parts of the point's impedance, respectively.

The features based on the information at fixed frequency points are the impedance values measured at 20 kHz ( $FF_{20k-Z}$ ), the real parts ( $FF_{1k-Z'}$ ,  $FF_{300k-Z'}$ ), and imaginary parts ( $FF_{1k-Z''}$ ,  $FF_{300k-Z''}$ ) of the impedance measured at 1 kHz and 300 kHz as Equations (6)–(8), respectively:

$$FF_{20k-Z,i} = \sqrt{R_{i,f}^2 + X_{i,f}^2} \quad \left( \begin{array}{l} i = 1, 2, \dots, 6 \text{ for ISA} \\ f = 20k \end{array} \right) \quad (6)$$

$$FF_{f-Z',i} = R_{i,n} \quad \left( \begin{array}{l} i = 1, 2, \dots, 6 \text{ for ISA} \\ f = 1k, 300k \end{array} \right) \quad (7)$$

$$FF_{f-Z'',i} = X_{i,n} \quad \left( \begin{array}{l} i = 1, 2, \dots, 6 \text{ for ISA} \\ f = 1k, 300k \end{array} \right) \quad (8)$$

where  $f$  is the frequency of the selected point in the Nyquist plot, and other variables are the same as in Equations (4) and (5).

In this contribution, the process of feature fusion was performed by fusing the features based on current and potential information for VSA and the features based on information of characteristic points and fixed frequency points for ISA, respectively. The features of the 4 sensors in the VSA were concatenated to form a 12-dimensional feature vector. Similarly, the features of the 6 sensors in the ISA were concatenated into a feature vector of 42 dimensionalities.

### 2.4.2. Dimensionality Reduction

Redundant correlations between each sensor in the array can result in a “curse of dimensionality” in case of excessive features [51]. Therefore, the extracted features can be projected into a low-dimensional space to obtain new principal variables without redundancy. Supervised dimensionality reduction algorithms are widely used in sensor array signal analysis [52]. In this study, linear discriminant analysis (LDA) was applied to reduce the dimensionality of the feature vectors.

The central idea of LDA is to minimize the intra-class spacing and maximize the inter-class variance after projection. The information of input data sets should also include the classes of the samples, so the input data set was  $X = \{(x_1, y_1), (x_2, y_2), \dots, (x_m, y_m)\}$ , where any sample  $x_i$  ( $i = 1, 2, \dots, m$ ) is an  $n$ -dimensional vector and  $y_i \in \{C_1, C_2, \dots, C_k\}$  is the classes (3 metallic ions and their 9 concentrations) of the samples.  $N_j$  ( $j = 1, 2, \dots, k$ ) is defined as the number of samples (30 repeat samples) in class  $j$ ,  $X_j$  ( $j = 1, 2, \dots, k$ ) as the vector set of samples in class  $j$ ,  $\mu_j$  ( $j = 1, 2, \dots, k$ ) as the mean vector of samples in class  $j$ , and  $\Sigma_j$  ( $j = 1, 2, \dots, k$ ) as the covariance matrix of samples in class  $j$ . The within-class scatter matrix  $S_w$  and the between-class scatter matrix  $S_b$  were calculated through the expressions (9) and (10) [53]:

$$S_w = \sum_{j=1}^k S_{wj} = \sum_{j=1}^k \sum_{x \in X_j} (x - \mu_j)(x - \mu_j)^T \quad (9)$$

$$S_b = \sum_{j=1}^k N_j (\mu_j - \mu)(\mu_j - \mu)^T \quad (10)$$

### 2.4.3. Classification

Classification is usually employed for further class identification of the dimensionality-reduced feature matrix. The supervised kNN classifier as a nonparametric statistics learning algorithm was applied in this contribution, which is a common classifier for signal processing of sensor arrays [54]. The classification of the test set data was determined by counting the major class of the  $k$  nearest samples in the feature space. The selected nearest samples should be previously correctly classified in a supervised manner.

### 2.4.4. Decision Fusion for Voltammetric and Impedimetric Measurements

Decision fusion integrates the recognition results from different sensor arrays to obtain higher prediction accuracy. Dempster–Shafer evidence theory (D–S evidence) is a general framework for reasoning with uncertainty and has been proven feasible for multi-sensor fusion in the literature [55].

$\Theta = \{\theta_1, \theta_2, \dots, \theta_c\}$  is defined as the discernment frame, and each class indicates a subset  $\theta_c$  ( $\theta_c \in \Theta$ ). The subjective probabilities (masses) are the key evidence of decision-making.  $A$  is a focal element of the discernment frame if the set function  $m : 2^\Theta \rightarrow [0, 1]$  is satisfied (11):

$$\begin{aligned} m(\phi) &= 0 \\ \sum_{A \in \Theta} m(A) &= 1 \end{aligned} \quad (11)$$

$m$  is then defined as the basic probability assignment in the discernment frame and  $m(A)$  as the probability assignment value [56]. A focal element is essentially a set of evidence derived from different sensor arrays. In this contribution, the VSA and ISA indicate two sets of evidence,  $m_1$  and  $m_2$ . Let the 27 classes of the samples be defined in the discernment frame as  $\Theta = \{\theta_1, \theta_2, \dots, \theta_{27}\}$ . The basic probability assignment function is obtained by the output of kNN.

The above two sets of evidence with  $A_1, A_2, \dots, A_i$  and  $B_1, B_2, \dots, B_j$  can be integrated into a new set of evidence  $m_{12}$  through D–S evidence combination rule (12) as follows:

$$m(A) = \frac{\sum_{A_i \cap B_j} m_1(A_i) m_2(B_j)}{1 - K} \quad A \neq \phi \quad (12)$$

where  $K = \sum_{A_i \cap B_j = \phi} m_1(A_i)m_2(B_j)$  and  $K < 1$  [56]. The final decision should be one of 27 classes, indicating the maximum membership of the plausibility. The algorithms were implemented by Python3 in PyCharm (JetBrains s.r.o., Prague, Czech Republic).

### 3. Results and Discussion

#### 3.1. Evaluation of Features

Radar plots (see Figure 2) are presented to observe whether pattern differences (i.e., fingerprints) arise between the sensors in the VSA and ISA response toward  $K^+$ ,  $Mg^{2+}$ , and  $Ca^{2+}$ . Responses of each sensor are presented as polygons composed of the extracted features. Overall, each sensor in both the VSA and the ISA exhibits significantly differentiated patterns in response to the three target analytes, i.e., polygons of different colors covering relatively different regions. These differences can be attributed to the effectiveness of the feature extraction and the cross-selectivity of the applied sensitive materials since the extracted features are all physically meaningful from CV and EIS curves and can characterize the sensors' response toward the analytes in multiple perspectives. These very differentiated patterns mean that the VSA and ISA have excellent properties, which have proven to be valuable for multi-analyte recognition in studies, e.g., volatile organic compounds [57], bio-analytes [58], and metal ions [59].

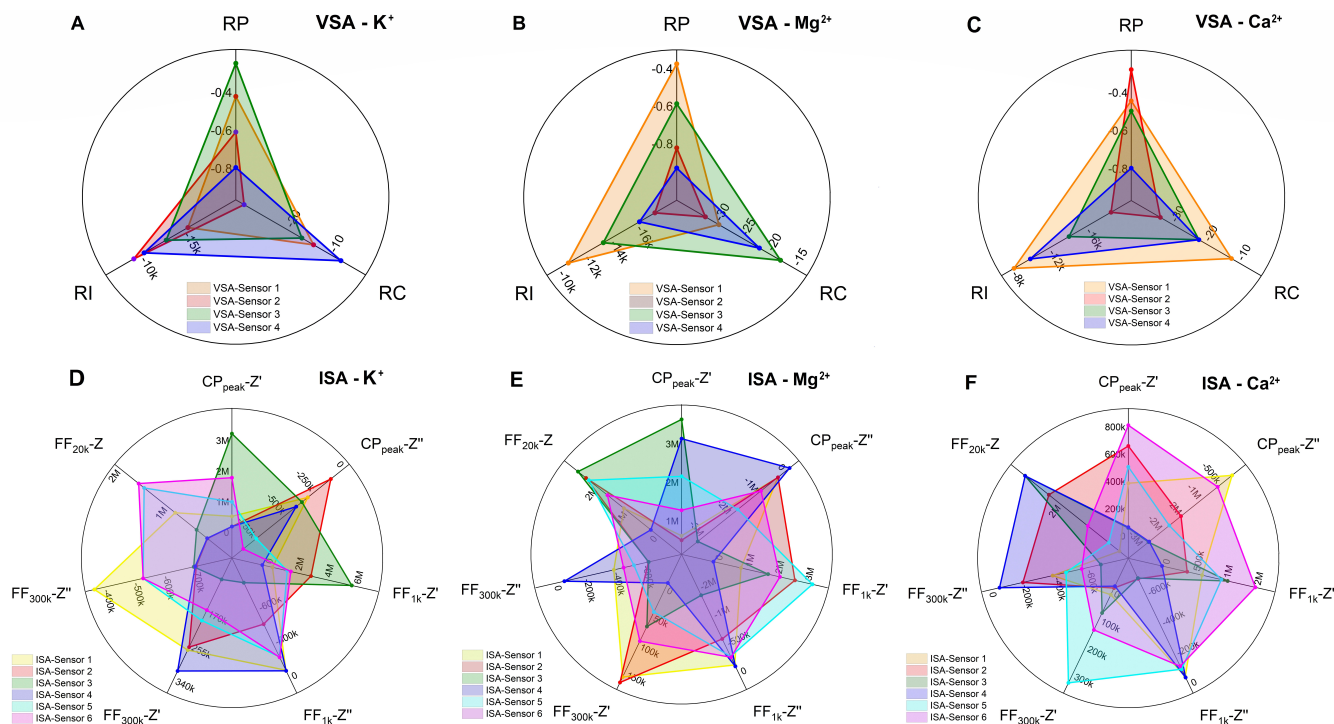


**Figure 2.** Extracted features of (A–C) VSA and (D–F) ISA towards  $K^+$ ,  $Mg^{2+}$ , and  $Ca^{2+}$  at a concentration of 50  $\mu M$ .

#### 3.2. Feature Fusion

The current features (RC, RI), potential features (RP), characteristic point features ( $CP_{peak-Z'}$ ,  $CP_{peak-Z''}$ ), and fixed frequency point features ( $FF_{20k-Z}$ ,  $FF_{1k-Z'}$ ,  $FF_{1k-Z''}$ ,  $FF_{300k-Z'}$ ,  $FF_{300k-Z''}$ ) were extracted from the acquired data of VSA and ISA according to Section 2.4.1, to more completely describe the response of the sensor arrays toward metal ions. The features were fused into two sets of feature vectors for VSA and ISA, respectively.

The score plot of the LDA displayed on the 2D plane can be applied for visual assessment of the recognition ability of the features. Less overlap in clusters of ion categories or concentrations means better recognition ability. Figures 3 and S3 show the score plots of the VSA considering based on the current features (Figures 3A,C and S3A,C)

and after feature fusion, that is, based on both the current and the potential features (Figures 3B,D and S3B,D).

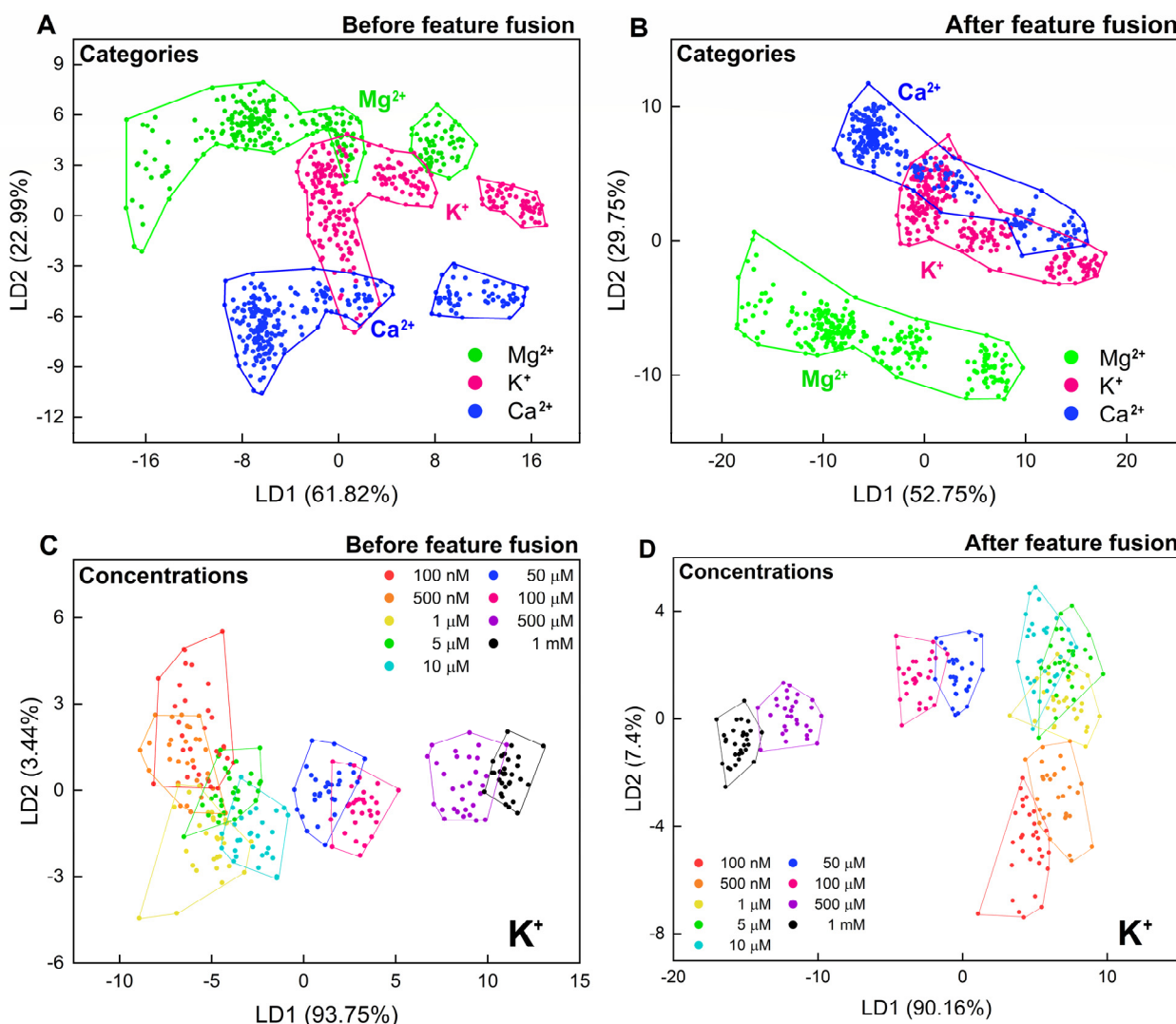


**Figure 3.** LDA score plots (2D) of the VSA for the discrimination of the metallic ions' categories and concentrations (K<sup>+</sup>) based on (A,C) only current features (before feature fusion) and (B,D) both current and potential features (after feature fusion), respectively.

In Figure 3A,B, the categories of metal ions are observed as clusters. The clusters of Mg<sup>2+</sup> and Ca<sup>2+</sup> overlap with the K<sup>+</sup> cluster considering only the current features, respectively; instead, the Mg<sup>2+</sup> is entirely independently distributed after feature fusion. The LDA scores of Ca<sup>2+</sup> and K<sup>+</sup> are partially overlapped due to dimensionality limitations, whereas they are entirely independent in higher dimensional space shown in next Section. The added potential features correlate with the ion categories, thus enhancing the qualitative recognition accuracy of the VSA.

The current features cannot distinguish well for different concentrations of K<sup>+</sup> (see Figure 3C). The overlapped boundaries reduce the correct recognition probability of the test samples. The clusters converge relatively after considering the potential features, and the boundaries are more clearly delineated (see Figure 3D). They mean that the quantitative recognition ability of VSA is relatively improved. Although the clusters of concentration range from 1.0 μM to 10.0 μM still overlap, the distribution becomes regular according to the increasing concentration. Additionally, the within-class samples distribute more compactly, which complies with the dimensionality reduction rule of LDA (Section 2.4.2). Similarly,

for the concentration discrimination of  $Mg^{2+}$  and  $Ca^{2+}$  (see Figure S3), the addition of the potential features results in the boundary condensing of each concentration's cluster.

Figures 4 and S4 show the score plots of ISA considering only the characteristic point features (see Figures 4A,C and S4A,C) and both characteristic point and fixed frequency point features, that is, after feature fusion (see Figures 4B,D and S4B,D). For the clusters of ion categories (see Figure 4A,B), more selected features enhance the distribution density of within-class scatters, especially for  $Mg^{2+}$ . The addition of the fixed frequency point features significantly improves the concentration discrimination of  $Mg^{2+}$  (Figure 4D), compared to discrimination only based on characteristic point features (see Figure 4C). Both between- and within-class distances converge significantly to the ideal states of LDA. Similarly, for  $K^+$  and  $Ca^{2+}$ , the concentration discrimination after feature fusion shows clearer boundaries (Figure S4).

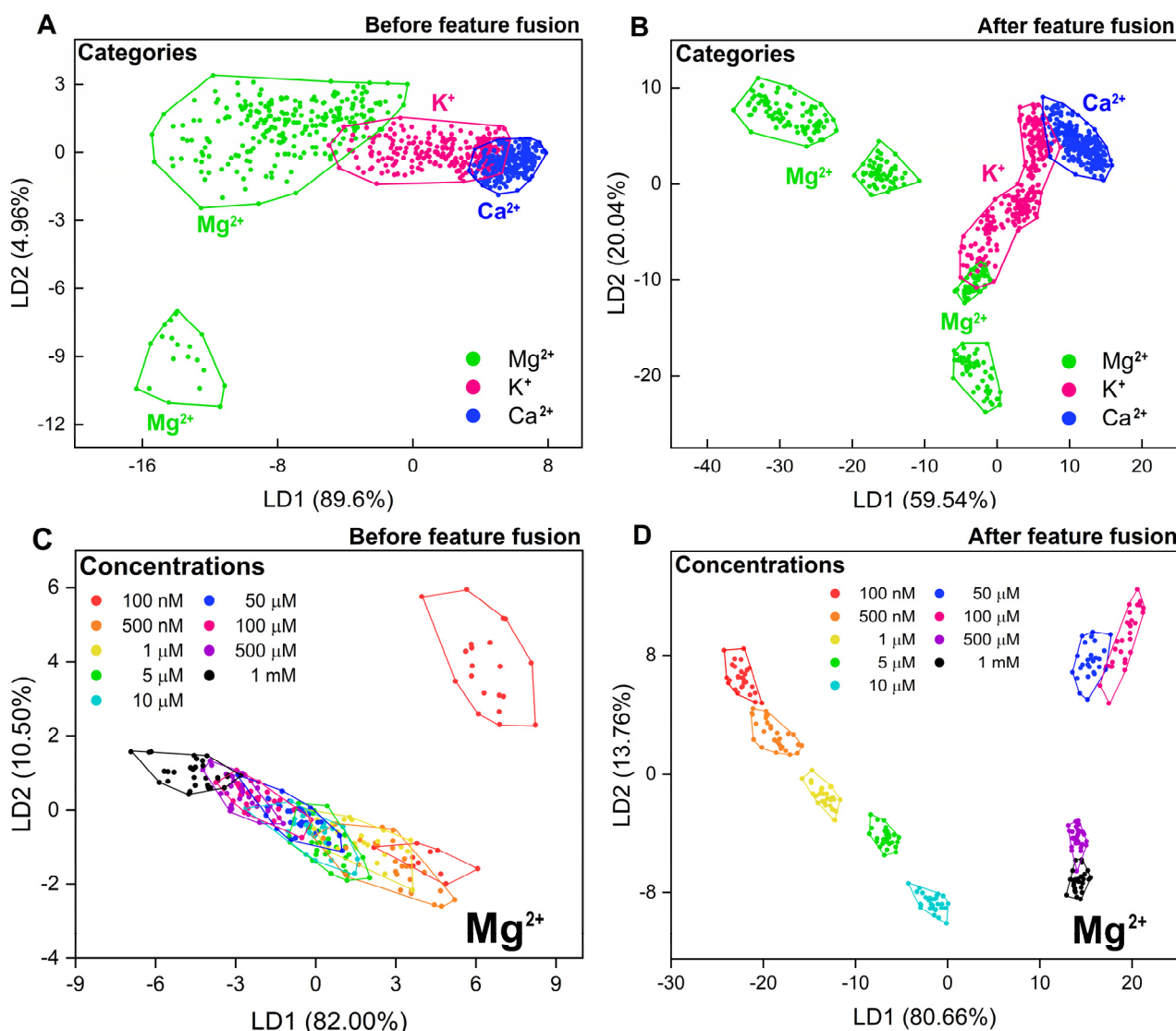


**Figure 4.** LDA score plots (2D) of the ISA for the discrimination of the metallic ions' categories and concentrations ( $Mg^{2+}$ ) based on (A,C) only characteristic point features (before feature fusion) and (B,D) both characteristic point and fixed frequency point features (after feature fusion).

The comparison of the quantitative recognition accuracies of VSA and ISA based on different features is presented in Figures S5 and S6. Higher accuracies are observed in most cases of recognition after feature fusion. The results of both VSA and ISA demonstrated the advantages of feature fusion in characterizing the comprehensive signal of sensors.

The vectors of multi-features better described the overall signals of the sensor array and improved the qualitative and quantitative prediction accuracy. The reason for ISA's better result is related to the number of added fixed-frequency features. More considered valuable features compared to the VSA can provide a more comprehensive recognition basis [60].

### 3.3. Dimensionality Reduction

The number of principal components (PC) in the dimensionality reduction process impacts the prediction accuracy [57,61]. This section studied the PC number's effect of LDA on the prediction accuracy of VSA and ISA toward ion categories (see Figure 5). Figure 5A,B demonstrate the score plots of VSA and ISA in 3D space composed of the first three PCs (LD1, LD2, LD3) of the LDA results and the eigenvalues and cumulative contributions of its PCs (scree plot). The cumulative contributions of VSA and ISA are 94.48% and 91.90%, respectively, which can represent the majority of the information of the fused feature vector. The cumulative contributions of the first six PCs are nearly 100%. Compared to the 2D plane (Figures 3B and 4B), the clusters representing ion categories are distributed independently in the 3D space due to the addition of the LD3 projection on the z-axis direction. Extending information in the 3D space provides more precise boundaries for the categories and improves prediction accuracy.

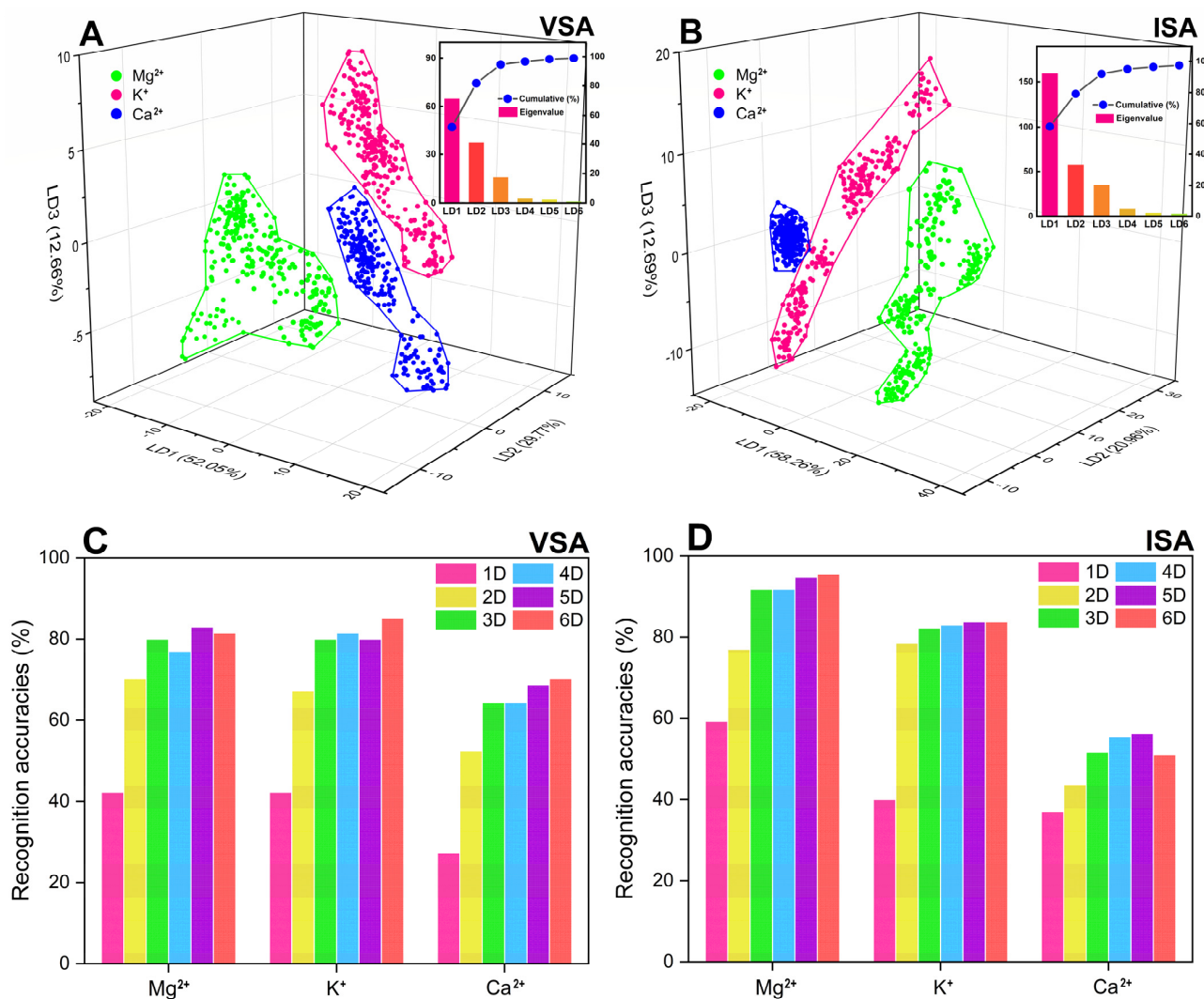


**Figure 5.** LDA score plots (3D) of (A) VSA and (B) ISA for discrimination of metallic ions' categories with scree plots (LD1 to LD6) as insets, and the recognition accuracies of (C) VSA and (D) ISA under 1D to 6D conditions.

The prediction accuracy of VSA and ISA toward ion categories in the 1D to 6D space is shown in Figure 5C,D, respectively. The predictions were performed by LDA only, and the training and testing set consisted of 405 samples each. The accuracies were relatively low under 1D and 2D due to the unclear boundaries of the clusters. From 3D to 6D, the accuracy no more increased significantly with increasing dimensions. The prediction accuracy for  $\text{Ca}^{2+}$  was relatively low (<70%) due to the performance limitations of the sensor array itself. The highest accuracies were 85.18% for  $\text{K}^+$  (VSA, 6D) and 95.55% for  $\text{Mg}^{2+}$  (ISA, 6D).

The results demonstrate that the LDA method is effective in the supervised classification of potassium, calcium, and magnesium ions. It can be applied for accurate and fast classification due to the simplicity of the computational process [53]. In addition, the results show that there is a difference in the recognition accuracy obtained by the ET when different PC numbers are considered. The LDA method has been employed by many researchers for the ET classification of metal ions. Li et al. [62] applied the LDA method in colorimetric ET for the determination of six metal ions. Similarly, Sipos et al. [63] and Men et al. [64] classified mineral water by determining contained ions through LDA-based ETs.

### 3.4. Classification

As an instance-based learning algorithm, the recognition accuracy of kNN is influenced by the k value (nearest neighbors) [65]. In this section, the classification effect of kNN on the reduced-dimensional samples and the impact of different combinations of k values and dimensions on the recognition accuracy were discussed (see Figure 6). Figure 6A,B demonstrate the classification effect of kNN ( $k = 5$ ) on the LDA-processed samples in the 2D plane. The training set (squares) and the testing set (stars) consist of 405 samples each. The different colored areas mean that if the testing sample is within them, it will be identified as the indicating ion category and concentration. For the VSA, the regions' area of the three metal ions are approximately the same, but  $\text{Ca}^{2+}$  was divided into two separate parts. Each region has clear boundaries, and the colored areas were arranged in a regular pattern according to the concentration changes. For ISA,  $\text{K}^+$  and  $\text{Mg}^{2+}$  were well classified, as well as the concentration regions in  $\text{Ca}^{2+}$  overlapped each other obviously, which can be improved at higher dimensions.

The choice of the k value usually depends on the data. A larger k value can reduce the influence of noise during classification but blurs the boundaries between categories [66]. Figure 6C,D show the impact of different combinations of dimensions (D: 1 to 6) and k value (k: 1 to 15) on the total recognition accuracy. In 1D and 2D space, the accuracy roughly increases with increasing k value. However, in the 3D–6D space, the accuracy remains at around 80% and is not influenced by the change in k. The optimal total recognition accuracies are 80.98% and 81.48% for VSA and ISA, respectively, both happening under the condition of  $D = 6$  and  $k = 5$ .

The obtained results showed that kNN could be efficiently applied to voltammetric and impedimetric ETs by adjusting the k value. KNN algorithm could be used for either classification or regression; therefore, it was employed by researchers in many valuable application fields of ETs, for example, the determination of wine [67], classification of tea [68], geographical origin identification of crops [69], etc.

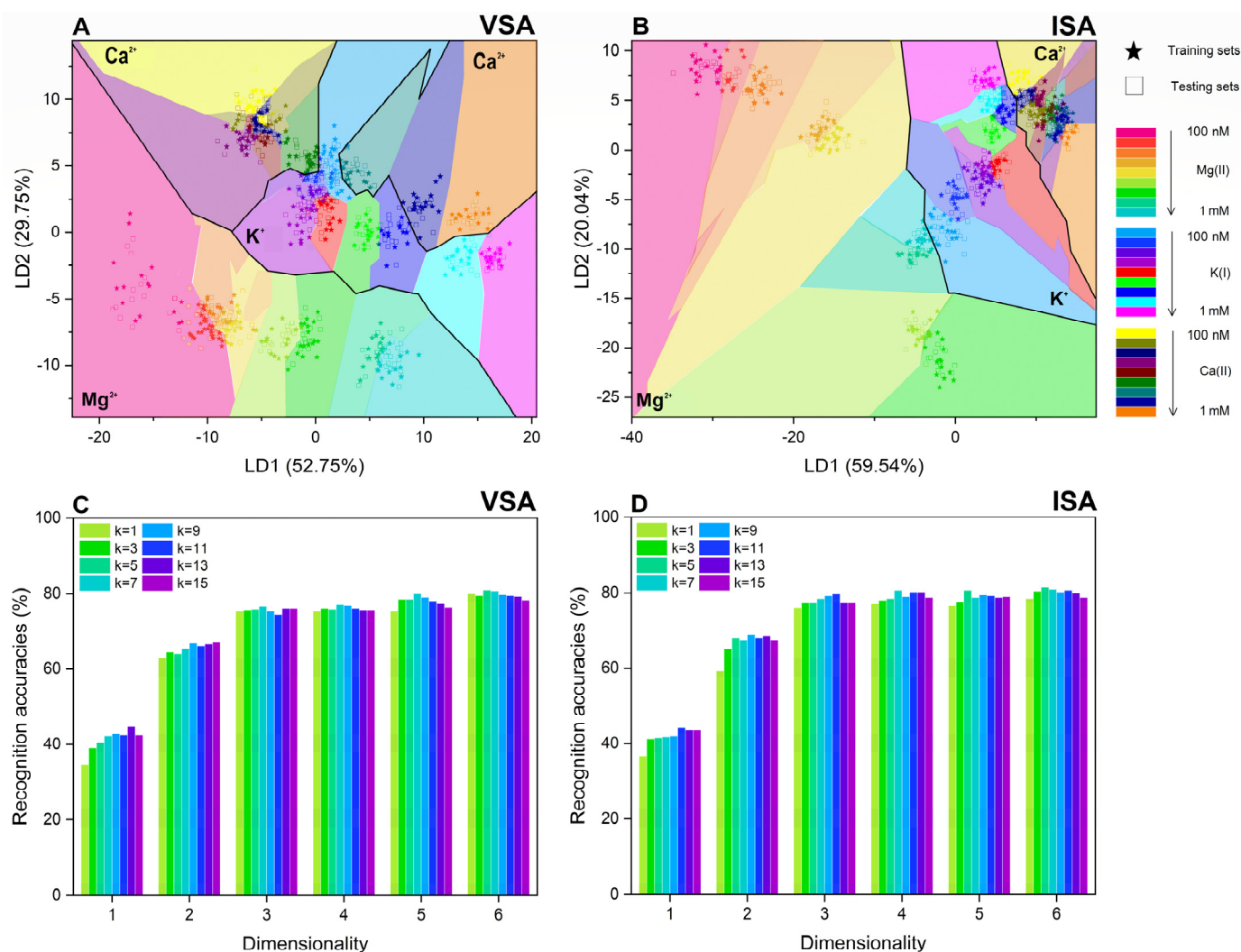


**Figure 6.** KNN ( $D = 2$ ,  $k = 5$ ) classification results of (A) VSA and (B) ISA with training and testing samples, and the effect of  $k$  value on total recognition accuracies of (C) VSA and (D) ISA.

### 3.5. Comparison of Algorithm Combinations

The effectiveness of the LDA-kNN combination was compared with other popular dimensionality reduction-classification combinations. The total prediction accuracy of different combinations of dimensionality reduction algorithms (LDA, principal component analysis (PCA), and isometric mapping (ISOMAP)) and classifiers (kNN, support vector machine (SVM), random forest (RF), and gradient boosting machine (GBM)) applied on VSA and ISA are shown in Figure 7.

For the dimensionality reduction algorithm, ISOMAP achieves a total accuracy of only 61% (with classifier kNN) due to it being more suitable for non-linear data structures. PCA, as an unsupervised algorithm, achieves a total accuracy of around 75%. LDA was proven to provide the highest recognition accuracy of over 80% due to its supervised model and optimal between/within class distances.

For the classifiers, the accuracy exceeds 70% in all combinations with LDA (kNN > RF > SVM > GBM). SVM is a non-probabilistic binary linear classifier based on model boundaries; thus, the complex scatters distribution reduces its recognition accuracy. In contrast, kNN with a small  $k$  value outperforms SVM for complex boundaries [70]. RF and GBM are ensemble methods more suitable for large-scale processing data [71]. Moreover, they require high computing power, which results in their unsuitability for real-time computing on portable devices. The best combination is LDA-kNN (80.98%), and

the worst is ISOMAP-GBM (52.59%). Overall, the dimensionality reduction algorithms affect the recognition accuracy more than the classifier.

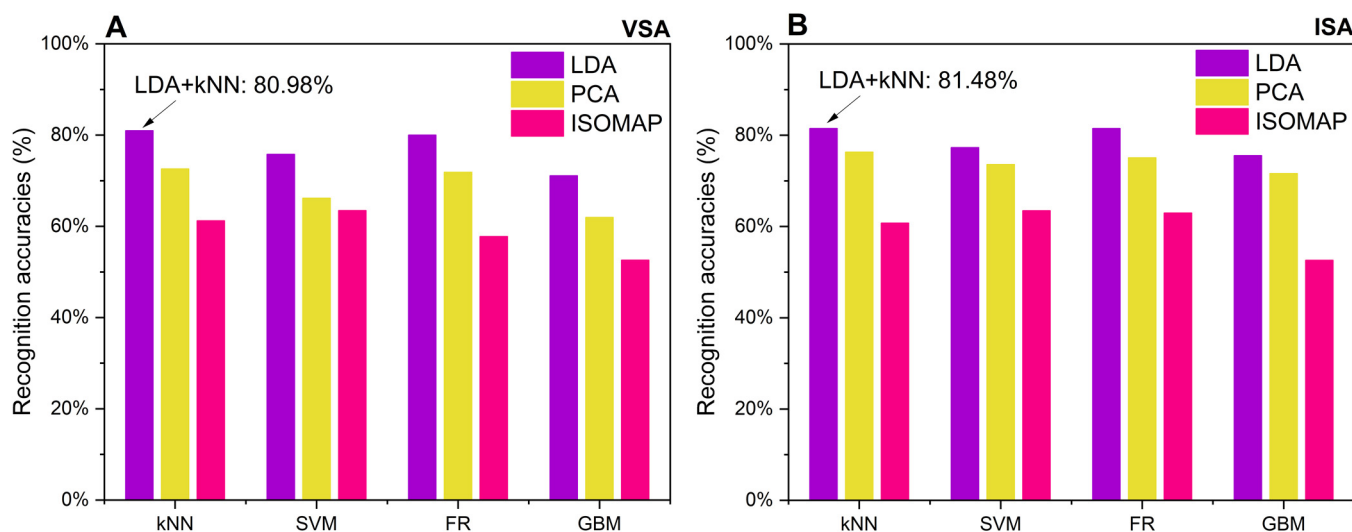


**Figure 7.** Recognition accuracies for (A) VSA and (B) ISA based on several combinations of dimensionality reduction—classification algorithms.

### 3.6. Quantitative Determination of Metallic Ions Based on Different Fusion Strategies

The LDA-kNN framework based on multi-features can improve the total recognition accuracy of VSA and ISA to approximately 80%. Nevertheless, it is not satisfactory for plant growth processes that require precise determination of metal ion concentrations. DS evidence theory is applied for decision-level fusion to obtain higher recognition accuracy. Based on the results in Section 3.4 regarding the optimal accuracy, the optimal parameters of both VSA and ISA were chosen as  $D = 6$  and  $k = 5$ .

Figures 8 and S7 show the confusion matrix and the recognition accuracy of ion categories, respectively, based on different fusion strategies. The total recognition accuracies of VSA and ISA after individual feature fusion are 80.98% (Figure 8A) and 81.48% (Figure 8B). The proposed multi-fusion based on individual feature fusion and DS evidence as decision fusion improved the total accuracy to 91.60% (Figure 8D). In comparison, the one-step feature fusion method, which combines all extracted voltammetric and impedimetric features together and makes only one decision, was tested, and total accuracy of 89.13% was obtained (Figure 8C). The diagonal line of the confusion matrix indicates the correct recognition of the 27 patterns (three categories  $\times$  nine concentrations), and the other elements indicate the misidentification between classes. For  $Mg^{2+}$ , the average recognition accuracy of VSA is 82.96%, while that of ISA is as high as 95.55%. After fusing the decisions, the accuracy improved to 97.78%. The accuracy of VSA and ISA for  $Ca^{2+}$  was 73.33% and 59.26%, respectively, and the decision fusion improved it to 82.96%. Especially for the relatively high concentration range (50  $\mu M$  to 1.0 mM), decision fusion corrected the misidentifications of ISA and improved the accuracy to 98.33%. The one-step feature fusion method showed a similar accuracy on  $Mg^{2+}$  compared to the multi-fusion approach but lower accuracy on  $K^+$  and  $Ca^{2+}$ . The above results demonstrate the effectiveness of DS evidence-based decision fusion in improving the recognition accuracy of VSA and ISA for the categories and concentrations of  $Mg^{2+}$ ,  $K^+$ , and  $Ca^{2+}$ .

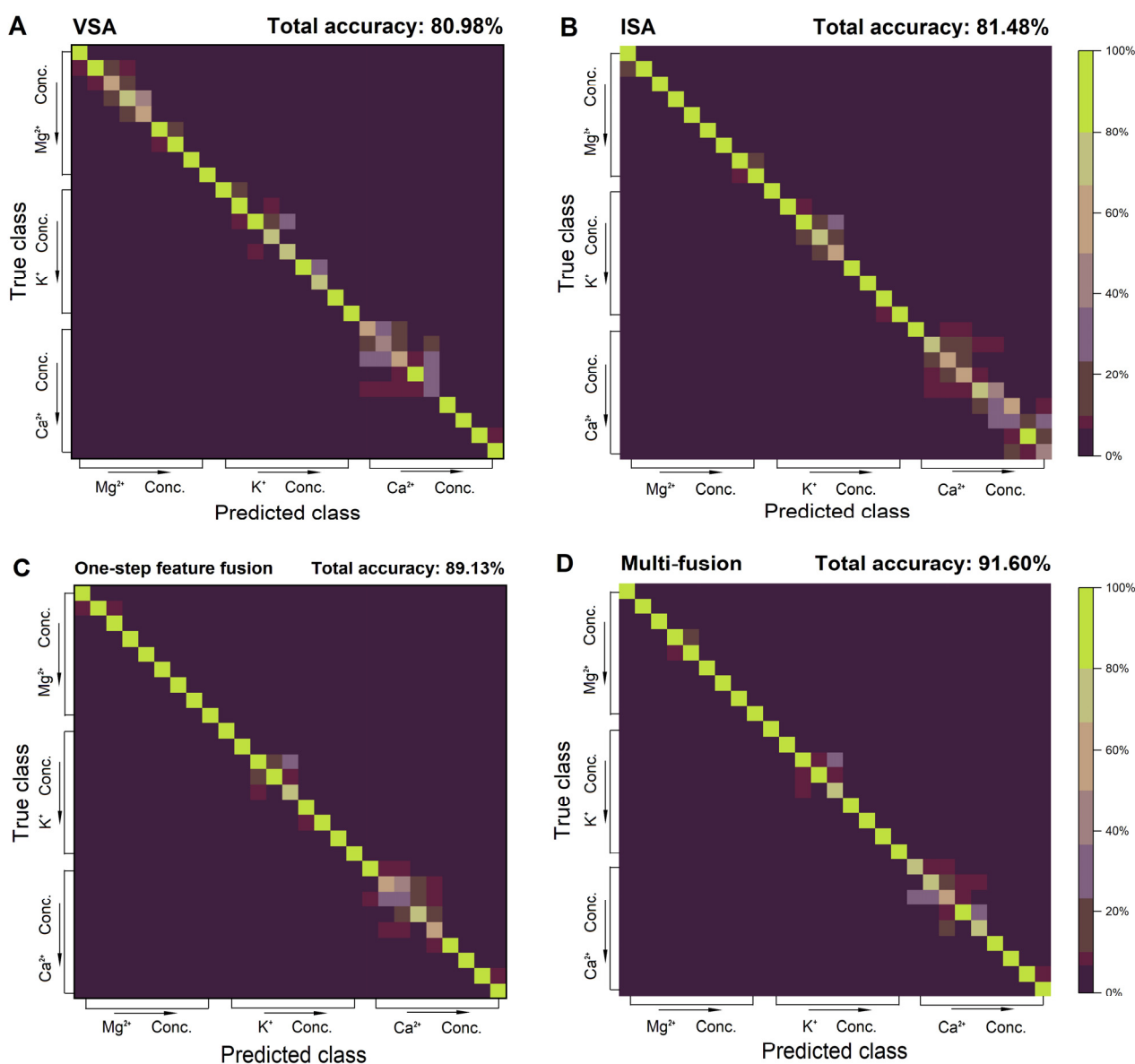


**Figure 8.** Confusion matrix of (A) VSA, (B) ISA, (C) only using one-step feature fusion, and (D) using multi-fusion under the optimal condition of  $D = 6$  and  $k = 5$  toward 100.0 nM to 1.0 mM of the  $K^+$ ,  $Mg^{2+}$ , and  $Ca^{2+}$ .

The obtained results reveal the application potential of the fusion of sensor arrays. Even the result based on one-step feature fusion is far preferable to the individual sensor arrays due to the inclusion of more observation dimensions. The fusion of sensor arrays based on different artificial senses (e.g., ET + EN, ET + EN + electronic eye (EE)) has been applied in many detection scenarios, especially in food evaluation, including ET + EN for evaluation of meat [72], olive oil [73], black tea [74], and ET + EN + EE for evaluation of green tea [75], red wine [76], and rice wine [77]. However, the sensor arrays fusion of the same artificial sense with different sensing principles has rarely been investigated. In particular, the fusion with the impedimetric sensor array is still in the initial stage until now.

#### 4. Conclusions

In this paper, we proposed a multi-level pattern fusion framework to improve the recognition accuracy of  $Mg^{2+}$ ,  $K^{2+}$ , and  $Ca^{2+}$  by hybridizing voltammetric and impedimetric sensor arrays. This framework provided sensor arrays' individual decisions based on the feature fusion and classifier LDA-kNN with optimized parameters, then fused them with DS evidence to realize decision fusion. The features extracted from the voltammetric and impedimetric measurement data were evaluated as satisfying the expectations of observing the measured samples from different perspectives. LDA score plots and statistics in 2D demonstrated that feature fusion enhances the qualitative/quantitative accuracy of VSA and ISA for metal ions. The qualitative accuracy of VSA and ISA increased significantly in 1D–3D, showing clearer boundaries and more projection information. The kNN-based classification results showed that both VSA and ISA have optimal total recognition accuracies of 80.98% and 81.48% at  $D = 6$  and  $k = 5$ . The recognition accuracies of some combinations of dimensionality reduction algorithms and classifiers were shown to verify that the proposed LDA-kNN combination is the optimal strategy. The proposed multi-fusion based on feature and DS evidence-based decision fusion enhanced the total recognition accuracy to 91.60%. This multi-fusion framework can characterize the voltammetric and impedimetric response of metal ions more comprehensively, which is the reason why this system outperforms single-feature methods or single sensor-arrays.

The proposed multi-level pattern fusion framework and the hybrid ET are the first studies to consider the fusion of voltammetric and impedimetric sensor arrays and bring new possibilities to apply them in analyte determination. This framework also has the potential to be extended to fuse other sensor array-based artificial senses technologies or to detect biomarkers, heavy metal ions, explosives, pesticides, and other important analytes.

**Supplementary Materials:** The following are available online at <https://www.mdpi.com/article/10.3390/chemosensors10110474/s1>, Table S1: The preparation details of the sensors in voltammetric sensor array (VSA), Table S2: The preparation details of the sensors in impedimetric sensor array (ISA), Figure S1: Setup of the voltammetric measurement: (A) the prepared VSA consists of 4 sensors and (B) schematic diagram of voltammetric measurement, Figure S2: Setup of the impedimetric measurement: (A) the prepared ISA consists of 6 sensors and (B) schematic diagram of impedimetric measurement, Figure S3: LDA score plots (2D) of the VSA for the concentrations discrimination of (A,B)  $Mg^{2+}$  and (C,D)  $Ca^{2+}$ , respectively, based on (A,C) current features and (B,D) both current and potential features (after feature fusion), Figure S4: LDA score plots (2D) of the ISA for the concentrations discrimination of (A,B)  $K^{+}$  and (C,D)  $Ca^{2+}$ , respectively, based on (A,C) characteristic point features and (B,D) both characteristic point and fixed frequency features (after feature fusion), Figure S5: Quantitative recognition accuracies (LDA, 3D) of VSA based on current features (before feature fusion) and both current and potential feature (after feature fusion), Figure S6: Quantitative recognition accuracies (LDA, 3D) of ISA based on characteristic point features (before feature fusion) and both characteristic point and fixed frequency point features (after feature fusion), Figure S7: Average recognition accuracies of VSA, ISA, one-step feature fusion, and multi-fusion toward  $Mg^{2+}$ ,  $K^{+}$ , and  $Ca^{2+}$ .

**Author Contributions:** Conceptualization, T.L. and A.A.-H.; methodology, T.L. and A.A.-H.; software, T.L. and J.H.; validation, J.H. and Y.L.; formal analysis, T.L. and A.A.-H.; investigation, J.H.; resources, O.K.; data curation, Y.L. and Y.Q.; writing—original draft preparation, T.L., A.A.-H. and O.K.; writing—review and editing, T.L., A.A.-H. and O.K.; visualization, T.L. and Y.Q.; supervision, O.K.; project administration, O.K. and A.A.-H.; funding acquisition, O.K. and A.A.-H. All authors have read and agreed to the published version of the manuscript.

**Funding:** T.L., A.A.-H. and O.K. acknowledge the financial support within the project Nutricion (no. 24119201, 1 January 2020–31 December 2022) funded by the Sächsische Aufbaubank (SAB). O.K. and A.A.-H. acknowledge the financial support of Deutsche Forschungsgemeinschaft (DFG) (PhotoSens project no. KA 1663/12-1, 1 February 2020–31 January 2023).

**Data Availability Statement:** Not Applicable.

**Conflicts of Interest:** The authors declare no conflict of interest.

## References

1. Uchida, R. Essential Nutrients for Plant Growth: Nutrient Functions and Deficiency Symptoms. In *Plant Nutrient Management in Hawaii's Soils, Approaches for Tropical and Subtropical Agriculture*; Silva, J.A., Uchida, R., Eds.; College of Tropical Agriculture and Human Resources, University of Hawaii at Manoa: Honolulu, HI, USA, 2000; pp. 31–55.
2. Tenkorang, F.; Lowenberg-DeBoer, J. Forecasting Long-Term Global Fertilizer Demand. *Nutr. Cycl. Agroecosyst.* **2009**, *83*, 233–247. [[CrossRef](#)]
3. Zörb, C.; Senbayram, M.; Peiter, E. Potassium in Agriculture—Status and Perspectives. *J. Plant Physiol.* **2014**, *171*, 656–669. [[CrossRef](#)] [[PubMed](#)]
4. Tränkner, M.; Tavakol, E.; Jákl, B. Functioning of Potassium and Magnesium in Photosynthesis, Photosynthate Translocation and Photoprotection. *Physiol. Plant.* **2018**, *163*, 414–431. [[CrossRef](#)]
5. Kirkby, E.A.; Pilbeam, D.J. Calcium as a Plant Nutrient. *Plant Cell Environ.* **1984**, *7*, 397–405. [[CrossRef](#)]
6. Poovaiah, B.W.; Reddy, A.S.N.; Leopold, A.C. Calcium Messenger System in Plants. *Crit. Rev. Plant Sci.* **1987**, *6*, 47–103. [[CrossRef](#)]
7. Mikula, K.; Izydorczyk, G.; Skrzypczak, D.; Mironiuk, M.; Moustakas, K.; Witek-Krowiak, A.; Chojnacka, K. Controlled Release Micronutrient Fertilizers for Precision Agriculture—A Review. *Sci. Total Environ.* **2020**, *712*, 136365. [[CrossRef](#)] [[PubMed](#)]
8. Aoren, G.I. Ideal Nutrient Productivities and Nutrient Proportions in Plant Growth. *Plant Cell Environ.* **1988**, *11*, 613–620. [[CrossRef](#)]
9. Ahn, T.I.; Son, J.E. Theoretical and Experimental Analysis of Nutrient Variations in Electrical Conductivity-Based Closed-Loop Soilless Culture Systems by Nutrient Replenishment Method. *Agronomy* **2019**, *9*, 649. [[CrossRef](#)]
10. Zaini, A.; Kurniawan, A.; Herdhiyanto, A.D. Internet of Things for Monitoring and Controlling Nutrient Film Technique (NFT) Aquaponic. In Proceedings of the 2018 International Conference on Computer Engineering, Network and Intelligent Multimedia (CENIM), Surabaya, Indonesia, 26–27 November 2018; pp. 167–171. [[CrossRef](#)]
11. Savvas, D.; Manos, G. Automated Composition Control of Nutrient Solution in Closed Soilless Culture Systems. *J. Agric. Eng. Res.* **1999**, *73*, 29–33. [[CrossRef](#)]
12. Akhter, F.; Siddiquei, H.R.; Alahi, M.E.E.; Mukhopadhyay, S.C. Recent Advancement of the Sensors for Monitoring the Water Quality Parameters in Smart Fisheries Farming. *Computers* **2021**, *10*, 26. [[CrossRef](#)]
13. Lavanaya, M.; Parameswari, R. Soil Nutrients Monitoring For Greenhouse Yield Enhancement Using Ph Value with Iot and Wireless Sensor Network. In Proceedings of the 2018 Second International Conference on Green Computing and Internet of Things (ICGCIoT), Bangalore, India, 16–18 August 2018; pp. 547–552. [[CrossRef](#)]
14. Pereira, C.M.; Neiverth, C.A.; Maeda, S.; Guiotoku, M.; Franciscon, L. Complexometric Titration with Potentiometric Indicator to Determination of Calcium and Magnesium in Soil Extracts. *Rev. Bras. Ciênc. Solo* **2011**, *35*, 1331–1336. [[CrossRef](#)]
15. De Caland, L.B.; Silveira, E.L.C.; Tubino, M. Determination of Sodium, Potassium, Calcium and Magnesium Cations in Biodiesel by Ion Chromatography. *Anal. Chim. Acta* **2012**, *718*, 116–120. [[CrossRef](#)] [[PubMed](#)]
16. Collins, D.; Lee, M. Developments in Ion Mobility Spectrometry–Mass Spectrometry. *Anal. Bioanal. Chem.* **2002**, *372*, 66–73. [[CrossRef](#)] [[PubMed](#)]
17. Wu, J.; Yu, J.; Li, J.; Wang, J.; Ying, Y. Detection of Metal Ions by Atomic Emission Spectroscopy from Liquid-Electrode Discharge Plasma. *Spectrochim. Acta Part B At. Spectrosc.* **2007**, *62*, 1269–1272. [[CrossRef](#)]
18. Bosch Ojeda, C.; Sanchez Rojas, F. Recent Applications in Derivative Ultraviolet/Visible Absorption Spectrophotometry: 2009–2011. *Microchem. J.* **2013**, *106*, 1–16. [[CrossRef](#)]
19. Nasraoui, S.; Al-Hamry, A.; Teixeira, P.R.; Ameer, S.; Paterno, L.G.; Ben Ali, M.; Kanoun, O. Electrochemical Sensor for Nitrite Detection in Water Samples Using Flexible Laser-Induced Graphene Electrodes Functionalized by CNT Decorated by Au Nanoparticles. *J. Electroanal. Chem.* **2021**, *880*, 114893. [[CrossRef](#)]
20. Talbi, M.; Al-Hamry, A.; Teixeira, P.R.; Paterno, L.G.; Ali, M.B.; Kanoun, O. Enhanced Nitrite Detection by a Carbon Screen Printed Electrode Modified with Photochemically-Made AuNPs. *Chemosensors* **2022**, *10*, 40. [[CrossRef](#)]
21. Brahem, A.; Al-Hamry, A.; Gross, M.A.; Paterno, L.G.; Ali, M.B.; Kanoun, O. Stability Enhancement of Laser-Scribed Reduced Graphene Oxide Electrodes Functionalized by Iron Oxide/Reduced Graphene Oxide Nanocomposites for Nitrite Sensors. *J. Compos. Sci.* **2022**, *6*, 221. [[CrossRef](#)]
22. Xiao, S.; Chen, L.; Xiong, X.; Zhang, Q.; Feng, J.; Deng, S.; Zhou, L. A New Impedimetric Sensor Based on Anionic Intercalator for Detection of Lead Ions with Low Cost and High Sensitivity. *J. Electroanal. Chem.* **2018**, *827*, 175–180. [[CrossRef](#)]
23. Chabbah, T.; Abderrazak, H.; Souissi, R.; Saint-Martin, P.; Casabianca, H.; Chatti, S.; Mercier, R.; Rassas, I.; Errachid, A.; Hammami, M.; et al. A Sensitive Impedimetric Sensor Based on Biosourced Polyphosphine Films for the Detection of Lead Ions. *Chemosensors* **2020**, *8*, 34. [[CrossRef](#)]
24. Bratov, A.; Abramova, N.; Ipatov, A. Recent Trends in Potentiometric Sensor Arrays—A Review. *Anal. Chim. Acta* **2010**, *678*, 149–159. [[CrossRef](#)] [[PubMed](#)]
25. Gruden, R.; Kanoun, O. Low-Cost Online Determination of Calcium-Magnesium-Ratio by Cyclic Voltammetry. In Proceedings of the 2014 IEEE 11th International Multi-Conference on Systems, Signals & Devices (SSD14), Castelldefels, Spain, 11–14 February 2014; pp. 1–3. [[CrossRef](#)]
26. Gruden, R.; Kanoun, O. Low-Cost Multifunctional Sensorsystem for Online Determination of Aqueous Solutions. In Proceedings of the 2015 IEEE 12th International Multi-Conference on Systems, Signals & Devices (SSD15), Mahdia, Tunisia, 22–25 March 2015; pp. 1–4. [[CrossRef](#)]

27. Peng, Z.; Cao, Y.; Gao, Y.; Wang, K.; Song, H.; Yan, S. Fabrication of NiS<sub>2</sub> Nanomaterial for Ca<sup>2+</sup>, Mg<sup>2+</sup> Sensing. In Proceedings of the International Conference on Optoelectronic and Microelectronic Technology and Application, Nanjing, China, 20–22 October 2020; Liu, J., Ed.; SPIE: Bellingham, WA, USA, 2020; p. 21. [\[CrossRef\]](#)
28. Kumbhat, S.; Singh, U. A Potassium-Selective Electrochemical Sensor Based on Crown-Ether Functionalized Self Assembled Monolayer. *J. Electroanal. Chem.* **2018**, *809*, 31–35. [\[CrossRef\]](#)
29. Akhter, F.; Nag, A.; Alahi, M.E.E.; Liu, H.; Mukhopadhyay, S.C. Electrochemical Detection of Calcium and Magnesium in Water Bodies. *Sens. Actuators A Phys.* **2020**, *305*, 111949. [\[CrossRef\]](#)
30. Machado, R.; Soltani, N.; Dufour, S.; Salam, M.; Carlen, P.; Genov, R.; Thompson, M. Biofouling-Resistant Impedimetric Sensor for Array High-Resolution Extracellular Potassium Monitoring in the Brain. *Biosensors* **2016**, *6*, 53. [\[CrossRef\]](#)
31. Podražka, M.; Bącznyńska, E.; Kundys, M.; Jeleń, P.; Witkowska Nery, E. Electronic Tongue—A Tool for All Tastes? *Biosensors* **2017**, *8*, 3. [\[CrossRef\]](#) [\[PubMed\]](#)
32. Tahara, Y.; Toko, K. Electronic Tongues—A Review. *IEEE Sens. J.* **2013**, *13*, 3001–3011. [\[CrossRef\]](#)
33. Riul, A.; dos Santos, D.S.; Wohnrath, K.; Di Tommazo, R.; Carvalho, A.C.P.L.F.; Fonseca, F.J.; Oliveira, O.N.; Taylor, D.M.; Mattoso, L.H.C. Artificial Taste Sensor: Efficient Combination of Sensors Made from Langmuir–Blodgett Films of Conducting Polymers and a Ruthenium Complex and Self-Assembled Films of an Azobenzene-Containing Polymer. *Langmuir* **2002**, *18*, 239–245. [\[CrossRef\]](#)
34. Riul, A.; Gallardo Soto, A.M.; Mello, S.V.; Bone, S.; Taylor, D.M.; Mattoso, L.H.C. An Electronic Tongue Using Polypyrrole and Polyaniline. *Synth. Met.* **2003**, *132*, 109–116. [\[CrossRef\]](#)
35. Cortinapuig, M.; Munozberbel, X.; Alonsolomillo, M.; Munozpascual, F.; Delvalle, M. EIS Multianalyte Sensing with an Automated SIA System—An Electronic Tongue Employing the Impedimetric Signal. *Talanta* **2007**, *72*, 774–779. [\[CrossRef\]](#)
36. Pérez-Ràfols, C.; Serrano, N.; Díaz-Cruz, J.M.; Ariño, C.; Esteban, M. A Screen-Printed Voltammetric Electronic Tongue for the Analysis of Complex Mixtures of Metal Ions. *Sens. Actuators B Chem.* **2017**, *250*, 393–401. [\[CrossRef\]](#)
37. Men, H.; Zou, S.; Li, Y.; Wang, Y.; Ye, X.; Wang, P. A Novel Electronic Tongue Combined MLAPS with Stripping Voltammetry for Environmental Detection. *Sens. Actuators B Chem.* **2005**, *110*, 350–357. [\[CrossRef\]](#)
38. Cavallari, M.R.; Braga, G.S.; da Silva, M.F.P.; Izquierdo, J.E.E.; Paterno, L.G.; Dirani, E.A.T.; Kymissis, I.; Fonseca, F.J. A Hybrid Electronic Nose and Tongue for the Detection of Ketones: Improved Sensor Orthogonality Using Graphene Oxide-Based Detectors. *IEEE Sens. J.* **2017**, *17*, 1971–1980. [\[CrossRef\]](#)
39. Markovic, M.; Dosen, S.; Popovic, D.; Graitmann, B.; Farina, D. Sensor Fusion and Computer Vision for Context-Aware Control of a Multi Degree-of-Freedom Prosthesis. *J. Neural Eng.* **2015**, *12*, 066022. [\[CrossRef\]](#) [\[PubMed\]](#)
40. Calvini, R.; Pigani, L. Toward the Development of Combined Artificial Sensing Systems for Food Quality Evaluation: A Review on the Application of Data Fusion of Electronic Noses, Electronic Tongues and Electronic Eyes. *Sensors* **2022**, *22*, 577. [\[CrossRef\]](#)
41. Banerjee, R.; Tudu, B.; Bandyopadhyay, R.; Bhattacharyya, N. A Review on Combined Odor and Taste Sensor Systems. *J. Food Eng.* **2016**, *190*, 10–21. [\[CrossRef\]](#)
42. Gutiérrez, J.M.; Haddi, Z.; Amari, A.; Bouchikhi, B.; Mimendia, A.; Cetó, X.; del Valle, M. Hybrid Electronic Tongue Based on Multisensor Data Fusion for Discrimination of Beers. *Sens. Actuators B Chem.* **2013**, *177*, 989–996. [\[CrossRef\]](#)
43. Winquist, F.; Holmin, S.; Krantz-Rülcker, C.; Wide, P.; Lundström, I. A Hybrid Electronic Tongue. *Anal. Chim. Acta* **2000**, *406*, 147–157. [\[CrossRef\]](#)
44. Söderström, C.; Rudnitskaya, A.; Legin, A.; Krantz-Rülcker, C. Differentiation of Four Aspergillus Species and One Zygosaccharomyces with Two Electronic Tongues Based on Different Measurement Techniques. *J. Biotechnol.* **2005**, *119*, 300–308. [\[CrossRef\]](#)
45. Kutyla-Olesiuk, A.; Nowacka, M.; Wesoly, M.; Ciosek, P. Evaluation of Organoleptic and Texture Properties of Dried Apples by Hybrid Electronic Tongue. *Sens. Actuators B Chem.* **2013**, *187*, 234–240. [\[CrossRef\]](#)
46. Labrador, R.H.; Masot, R.; Alcañiz, M.; Baigts, D.; Soto, J.; Martínez-Mañez, R.; García-Breijo, E.; Gil, L.; Barat, J.M. Prediction of NaCl, Nitrate and Nitrite Contents in Minced Meat by Using a Voltammetric Electronic Tongue and an Impedimetric Sensor. *Food Chem.* **2010**, *122*, 864–870. [\[CrossRef\]](#)
47. Hira, Z.M.; Gillies, D.F. A Review of Feature Selection and Feature Extraction Methods Applied on Microarray Data. *Adv. Bioinform.* **2015**, *2015*, 198363. [\[CrossRef\]](#) [\[PubMed\]](#)
48. Nasraoui, S.; Ameer, S.; Al-Hamry, A.; Ben Ali, M.; Kanoun, O. Development of an Efficient Voltammetric Sensor for the Monitoring of 4-Aminophenol Based on Flexible Laser Induced Graphene Electrodes Modified with MWCNT-PANI. *Sensors* **2022**, *22*, 833. [\[CrossRef\]](#)
49. Gruden, R.; Buchholz, A.; Kanoun, O. Electrochemical Analysis of Water and Suds by Impedance Spectroscopy and Cyclic Voltammetry. *J. Sens. Sens. Syst.* **2014**, *3*, 133–140. [\[CrossRef\]](#)
50. Al-Hamry, A.; Panzardi, E.; Mugnaini, M.; Kanoun, O. Health Monitoring of Human Breathing by Graphene Oxide Based Sensors. In Proceedings of the Sensors and Measuring Systems: 19th ITG/GMA-Symposium, Nuremberg, Germany, 26–27 June 2018; Volume 4.
51. Verleysen, M.; François, D. The Curse of Dimensionality in Data Mining and Time Series Prediction. In *Computational Intelligence and Bioinspired Systems*; Cabestany, J., Prieto, A., Sandoval, F., Eds.; Lecture Notes in Computer Science; Springer: Berlin/Heidelberg, Germany, 2005; Volume 3512, pp. 758–770, ISBN 978-3-540-26208-4. [\[CrossRef\]](#)
52. Ghriissi, H.; Veloso, A.C.A.; Marx, Í.M.G.; Dias, T.; Peres, A.M. A Potentiometric Electronic Tongue as a Discrimination Tool of Water-Food Indicator/Contamination Bacteria. *Chemosensors* **2021**, *9*, 143. [\[CrossRef\]](#)

53. Yu, H.; Yang, J. A Direct LDA Algorithm for High-Dimensional Data—With Application to Face Recognition. *Pattern Recognit.* **2001**, *34*, 2067–2070. [[CrossRef](#)]
54. Yang, J.; Sun, Z.; Chen, Y. Fault Detection Using the Clustering-KNN Rule for Gas Sensor Arrays. *Sensors* **2016**, *16*, 2069. [[CrossRef](#)] [[PubMed](#)]
55. Lin, T.-C. Improving D-S Evidence Theory for Data Fusion System. *Wu Feng J.* **2007**, *13*, 263–276.
56. Sentz, K.; Ferson, S. Combination of Evidence in Dempster-Shafer Theory. Ph.D. Thesis, Binghamton University, Binghamton, NY, USA, 2002.
57. Lu, T.; Al-Hamry, A.; Rosolen, J.M.; Hu, Z.; Hao, J.; Wang, Y.; Adiraju, A.; Yu, T.; Matsubara, E.Y.; Kanoun, O. Flexible Impedimetric Electronic Nose for High-Accurate Determination of Individual Volatile Organic Compounds by Tuning the Graphene Sensitive Properties. *Chemosensors* **2021**, *9*, 360. [[CrossRef](#)]
58. Mei, Y.; Zhang, Q.-W.; Gu, Q.; Liu, Z.; He, X.; Tian, Y. Pillar[5]Arene-Based Fluorescent Sensor Array for Biosensing of Intracellular Multi-Neurotransmitters through Host–Guest Recognitions. *J. Am. Chem. Soc.* **2022**, *144*, 2351–2359. [[CrossRef](#)]
59. Lu, T.; Al-Hamry, A.; Talbi, M.; Zhang, J.; Adiraju, A.; Hou, M.; Kanoun, O. Functionalized PEDOT:PSS Based Sensor Array for Determination of Metallic Ions in Smart Agriculture. In Proceedings of the 2021 6th International Conference on Nanotechnology for Instrumentation and Measurement (NanofIM), Opole, Poland, 25 November 2021; pp. 1–4.
60. Ross, A.; Jain, A. Information Fusion in Biometrics. *Pattern Recognit. Lett.* **2003**, *24*, 2115–2125. [[CrossRef](#)]
61. Bader, O.; Haddad, D.; Kallel, A.Y.; Hassine, T.; Amara, N.E.B.; Kanoun, O. Identification of Communication Cables Based on Scattering Parameters and a Support Vector Machine Algorithm. *IEEE Sens. Lett.* **2021**, *5*, 1–4. [[CrossRef](#)]
62. Li, X.; Li, S.; Liu, Q.; Chen, Z. Electronic-Tongue Colorimetric-Sensor Array for Discrimination and Quantitation of Metal Ions Based on Gold-Nanoparticle Aggregation. *Anal. Chem.* **2019**, *91*, 6315–6320. [[CrossRef](#)] [[PubMed](#)]
63. Sipos, L.; Kovács, Z.; Sági-Kiss, V.; Csiki, T.; Kókai, Z.; Fekete, A.; Héberger, K. Discrimination of Mineral Waters by Electronic Tongue, Sensory Evaluation and Chemical Analysis. *Food Chem.* **2012**, *135*, 2947–2953. [[CrossRef](#)] [[PubMed](#)]
64. Men, H.; Ge, Z.; Guo, Y.; An, L.; Peng, Y. Biomimetic Electronic Tongue for Classification of Mineral Water. In Proceedings of the 2009 International Conference on Measuring Technology and Mechatronics Automation, Zhangjiajie, China, 11–12 April 2009; pp. 621–624.
65. Li, W.; Yi, P.; Wu, Y.; Pan, L.; Li, J. A New Intrusion Detection System Based on KNN Classification Algorithm in Wireless Sensor Network. *J. Electr. Comput. Eng.* **2014**, *2014*, 240217. [[CrossRef](#)]
66. Everitt, B.S.; Landau, S.; Leese, M.; Stahl, D. *Cluster Analysis: Wiley Series in Probability and Statistics*, 5th ed.; Wiley: Chichester, UK, 2011; ISBN 978-0-470-74991-3.
67. Śliwińska, M.; Garcia-Hernandez, C.; Kościński, M.; Dymerski, T.; Wardencki, W.; Namieśnik, J.; Śliwińska-Bartkowiak, M.; Jurga, S.; Garcia-Cabazon, C.; Rodriguez-Mendez, M. Discrimination of Apple Liqueurs (Nalewka) Using a Voltammetric Electronic Tongue, UV-Vis and Raman Spectroscopy. *Sensors* **2016**, *16*, 1654. [[CrossRef](#)]
68. Banerjee, M.B.; Roy, R.B.; Tudu, B.; Bandyopadhyay, R.; Bhattacharyya, N. Cross-Perception Fusion Model of Electronic Nose and Electronic Tongue for Black Tea Classification. In *Computational Intelligence, Communications, and Business Analytics*; Mandal, J.K., Dutta, P., Mukhopadhyay, S., Eds.; Communications in Computer and Information Science; Springer: Singapore, 2017; Volume 775, pp. 407–415, ISBN 978-981-10-6426-5.
69. Teye, E.; Huang, X.; Han, F.; Botchway, F. Discrimination of Cocoa Beans According to Geographical Origin by Electronic Tongue and Multivariate Algorithms. *Food Anal. Methods* **2014**, *7*, 360–365. [[CrossRef](#)]
70. Hamilton, D.; Pacheco, R.; Myers, B.; Peltzer, B. KNN vs. SVM: A Comparison of Algorithms. In Proceedings of the Fire Continuum-Preparing for the Future of Wildland Fire, Missoula, MT, USA, 21–24 May 2018; Hood, S.M., Drury, S., Steelman, T., Eds.; US Department of Agriculture, Forest Service, Rocky Mountain Research Station: Fort Collins, CO, USA, 2020; pp. 95–109.
71. Liu, Y. Random Forest Algorithm in Big Data Environment. *Comput. Model. New Technol.* **2014**, *18*, 147–151.
72. Tian, X.; Wang, J.; Ma, Z.; Li, M.; Wei, Z. Combination of an E-Nose and an E-Tongue for Adulteration Detection of Minced Mutton Mixed with Pork. *J. Food Qual.* **2019**, *2019*, 4342509. [[CrossRef](#)]
73. Haddi, Z.; Alami, H.; El Bari, N.; Tounsi, M.; Barhoumi, H.; Maaref, A.; Jaffrezic-Renault, N.; Bouchikhi, B. Electronic Nose and Tongue Combination for Improved Classification of Moroccan Virgin Olive Oil Profiles. *Food Res. Int.* **2013**, *54*, 1488–1498. [[CrossRef](#)]
74. Banerjee, M.B.; Roy, R.B.; Tudu, B.; Bandyopadhyay, R.; Bhattacharyya, N. Black Tea Classification Employing Feature Fusion of E-Nose and E-Tongue Responses. *J. Food Eng.* **2019**, *244*, 55–63. [[CrossRef](#)]
75. Xu, M.; Wang, J.; Zhu, L. The Qualitative and Quantitative Assessment of Tea Quality Based on E-Nose, E-Tongue and E-Eye Combined with Chemometrics. *Food Chem.* **2019**, *289*, 482–489. [[CrossRef](#)]
76. Prieto, N.; Gay, M.; Vidal, S.; Aagaard, O.; de Saja, J.A.; Rodriguez-Mendez, M.L. Analysis of the Influence of the Type of Closure in the Organoleptic Characteristics of a Red Wine by Using an Electronic Panel. *Food Chem.* **2011**, *129*, 589–594. [[CrossRef](#)] [[PubMed](#)]
77. Ouyang, Q.; Zhao, J.; Chen, Q. Instrumental Intelligent Test of Food Sensory Quality as Mimic of Human Panel Test Combining Multiple Cross-Perception Sensors and Data Fusion. *Anal. Chim. Acta* **2014**, *841*, 68–76. [[CrossRef](#)] [[PubMed](#)]